

Simultaneous Estimation of Near IR BRDF and Fine-Scale Surface Geometry

Gyeongmin Choe¹ Srinivasa G. Narasimhan² In So Kweon¹
Korea Advanced Institute of Science and Technology (KAIST)¹
Carnegie Mellon University (CMU)²

gmchoe@rcv.kaist.ac.kr srinivas@cs.cmu.edu iskweon77@kaist.ac.kr

Abstract

Near-Infrared (NIR) images of most materials exhibit less texture or albedo variations making them beneficial for vision tasks such as intrinsic image decomposition and structured light depth estimation. Understanding the reflectance properties (BRDF) of materials in the NIR wavelength range can be further useful for many photometric methods including shape from shading and inverse rendering. However, even with less albedo variation, many materials e.g. fabrics, leaves, etc. exhibit complex fine-scale surface detail making it hard to accurately estimate BRDF. In this paper, we present an approach to simultaneously estimate NIR BRDF and fine-scale surface details by imaging materials under different IR lighting and viewing directions. This is achieved by an iterative scheme that alternately estimates surface detail and NIR BRDF of materials. Our setup does not require complicated gantries or calibration and we present the first NIR dataset of 100 materials including a variety of fabrics (knits, weaves, cotton, satin, leather), and organic (skin, leaves, jute, trunk, fur) and inorganic materials (plastic, concrete, carpet). The NIR BRDFs measured from material samples are used with a shape-from-shading algorithm to demonstrate fine-scale reconstruction of objects from a single NIR image.

1. Introduction

Since the introduction of active 3D sensors like Microsoft Kinect, NIR imaging is becoming increasingly popular. Compared to the images in visible spectrum, NIR images of most materials exhibit much less texture (or albedo) variations making them suitable for tasks such as shadow detection [32], intrinsic image decomposition [21] and structured light based depth recovery [6]. However, the precise reflectance properties (*i.e.* BRDF [28]) of materials in the NIR wavelength range are not well understood. Measuring and modeling the BRDFs of materials will additionally make NIR imaging useful for a range of photometry based approaches such as shape from shading and inverse rendering.

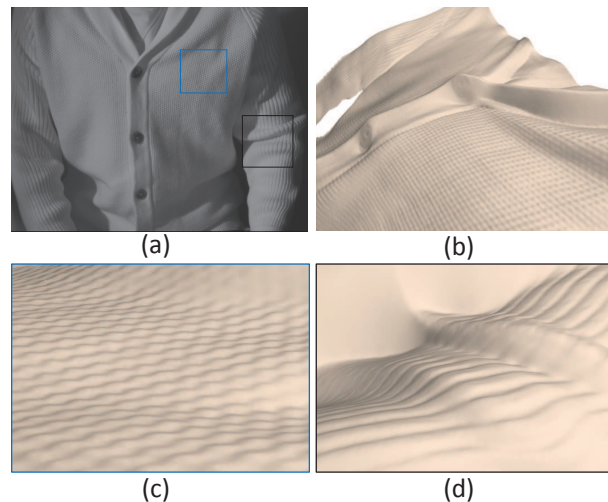


Figure 1. Fine-scale shape reconstruction from a single NIR image of a sweater made of cotton and polyester. We simultaneously estimate the surface detail and BRDF of over 100 material samples and use the BRDF obtained in a shape-from-shading method. (a) Input NIR image. (b) Rotated view of the 3D mesh. (c) Surface details on the chest. (d) Surface details on the arm. Both types of knits are well reconstructed.

BRDF estimation is well studied in the visible domain using both parametric [37, 30] and non-parametric approaches [8, 27, 2, 1]. Several datasets such as CURET [8] and MERL [27] have had a strong impact on photometry based research. In our work, Instead of using simple or known (spheres, planar patches, etc.) [26] objects, we target natural objects with fine surface geometries.

Our goal is to build a NIR database of real-world materials which contains NIR images captured under various lighting directions, corresponding surface normal maps and the BRDF models. The NIR domain offers both advantages and challenges. Since materials like fabrics appear (mostly) textureless, the BRDF remains constant spatially over at least small patches of materials. Both organic materials like leaves, tree trunks, and inorganic materials like knit and woven fabrics all show complex random or structural surface detail. These fine-scale surface height variations are diffi-

cult to measure or model [20] and pose challenges regardless of whether the NIR and visible wavelength spectra. We present a photometric stereo-based approach to jointly estimate both the NIR BRDF and the fine scale surface detail from images of material samples captured under different (known) lighting and viewing directions. This is achieved using an iterative approach that alternately estimates per-pixel surface normals and per-sample BRDFs. We restrict ourselves to materials that have a measurable diffuse component (so we do not measure metals or mirrors). This allows us to start the iterative process by assuming the material is simply Lambertian. Begin from the surface normal of the photometric stereo, the BRDF curve is fitted. We fit the data to a simple low-dimensional model parameterized by half angles [33] that was sufficient to represent all the materials we measured.

Using this approach, we measured the NIR BRDF and surface detail of over 100 materials that includes various types of fabrics (cotton, polyester, leather, satin etc.), leaves, papers, plastic, stones and concrete, etc. Each material sample was imaged under 12 different lighting directions and 9 different viewpoints. Despite the few combinations of lights and views, the BRDF is densely sampled due to the intricate surface detail. Our setup is very simple without requiring complicated gantries that are usually needed to densely sample BRDFs. We use the measured BRDF within a shape-from-shading algorithm to reconstruct a variety of different scenes (for example, people wearing different types of clothing) from a single NIR image under known lighting. Figure 1 shows the result of applying the shape from shading approach for fine-scale reconstruction of a sweater made of cotton and polyester with two different knit structures (checker and longitudinal). To our knowledge, the NIR BRDF and surface detail is the first such dataset and is publicly disseminated.

2. Related Work

Near IR imaging: Near IR imaging has been increasingly used for various computer vision tasks. In [34, 25, 36], NIR and visible images are jointly captured. The NIR image has unique characteristics compared to visible image and is used for scene understanding [5] and shadow detection [32]. In [21], NIR and visible images are used to compute an illumination invariant. NIR images have been used in various 3D applications such as enhancing depth quality or refining geometry of 3D meshes [6, 15]. These works show the NIR image is not affected by general indoor (ambient) lighting, which makes the lighting model simpler.

Material BRDF Estimation: BRDF estimation has been extensively addressed in the past decades. Beginning with the Lambertian model [22], various models based on empirical observations are presented such as Phong [31] and Schlick [35]. Torrance-Sparrow [37, 7], Oren-Nayar [30]

and Ward [39] have analyzed the physical properties of the materials with micro-surface roughness. These parametric BRDF models are based on physical light transport, however, they do not fully represent a wide range of real-world material properties. Alternative approaches measure the reflectance properties using measurement devices such as reflectometers [9, 11]. Nishino [29] presents the directional statistics based BRDF model and proposes to reduce the dimensions of BRDF data. Matusik *et al.* [27] present a generative model for isotropic BRDF via a data-driven approach. They acquire reflectance data by using spheres coated or attached with different materials. In CURET [8], novel bidirectional texture function (BTF) and BRDF are analyzed. They use 60 different samples of real-world materials and measure 200 combinations of viewing and illumination directions. Although they analyze various real-world material samples, they average the observed value over the plane to compute the BRDF.

Shape Estimation: BRDF models have been extensively used for shape from shading in the visible wavelength range. Shape from shading is an ill-posed problem and many restrictions and constraints are assumed [42, 3]. Beginning from numerical shape from shading [18, 16], various works rely on the Lambertian BRDF. Tsai *et al.* [38] uses discrete approximation for surface normal. Lee and Kuo [23] use triangular element surface model. The shape from shading methods are compared and evaluated in [41]. In [12], they utilize the photometric stereo and deal with both diffuse and specular surfaces. The parametric reflectance described in [4] is used in [17, 19]. In [17], they use a first-order approximation for the parameters and have bilinear reflectance, whereas, [19] uses second-order approximation for the parameters and have a quadratic one. Lensch *et al.* [24] present a generalized method for modeling non-Lambertian surfaces by using wavelet-based BRDFs. Several works exploit the depth sensor [13] as a prior for shape estimation. In [14, 40], they generate high-quality mesh model by estimating the natural illumination and combining it with depth from Kinect. Joint estimation of shape and reflectance based on the DSBRDF model [29] has demonstrated results for synthetic and real objects with smooth and simple shapes. In contrast, our work focuses on BRDF and surface detail estimation in NIR domain.

3. Data Acquisition

This section describes our measurement setup and data collection. Compared to conventional methods, our setup is more practical and does not require devices such as robot arms, high-speed cameras or reflectometers. Also typical indoor ambient light (fluorescent bulbs) do not affect the NIR capture process. The experimental setup is shown in Figure 2.

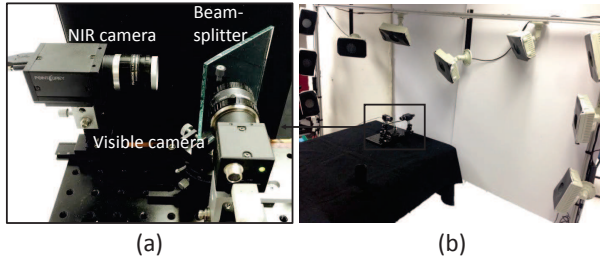


Figure 2. (a) Our acquisition setup. The NIR camera and the visible camera are co-located via beam-splitter. (b) 12 NIR light sources mounted at different locations. Note that our methods only requires the NIR camera and the visible camera is only used for visual comparisons but the data can be used for further research.

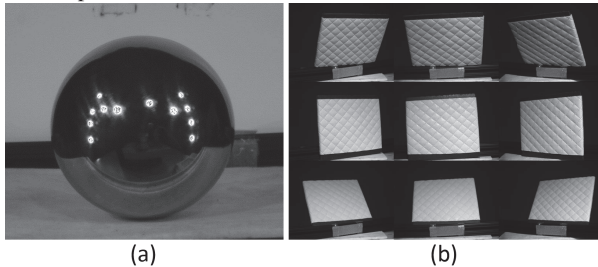


Figure 3. The lighting directions and viewing angles for one material sample (artificial leather). (a) 12 NIR distant point lightings reflected on the chrome ball. (b) 9 different viewing angles of the sample under one light direction.

3.1. Measurement Setup

Our setup consists of 12 IR LED sources and a near IR camera. We co-locate the NIR camera with a visible spectrum camera. The visible camera is not used for our algorithms, but only used for visual comparisons of the images. We use a pointgrey GS3-U3-41C6NIR-C camera with an IR pass filter that blocks visible light under the wavelength of $760nm$ (see supplementary material for spectral sensitivity of the camera). As seen in Figure 2, we co-locate the cameras with the beam-splitter and register the images using a homography transformation. After setting up our device for measurement, we collect real-world samples of different types of materials. As seen in Figure 3, the material samples are attached to a $10cm$ high and $13cm$ wide rectangular board. Both NIR and visible cameras are calibrated and undistorted.

3.2. NIR BRDF Database

Each material sample is tilted to 9 different angles w.r.t the camera and imaged under 12 different lighting directions, giving a total of 108 images of size 1600×1200 pixels. Assuming that the BRDF is constant spatially across the material sample, each image provides a dense set of BRDF samples. We have collected 100 real-world materials that include various types of fabrics (cotton, polyester, leather, satin, jute etc.), leaves, papers, plastic, stone, carpets, tree trunk, furs, human skin and concretes etc. A complete list-

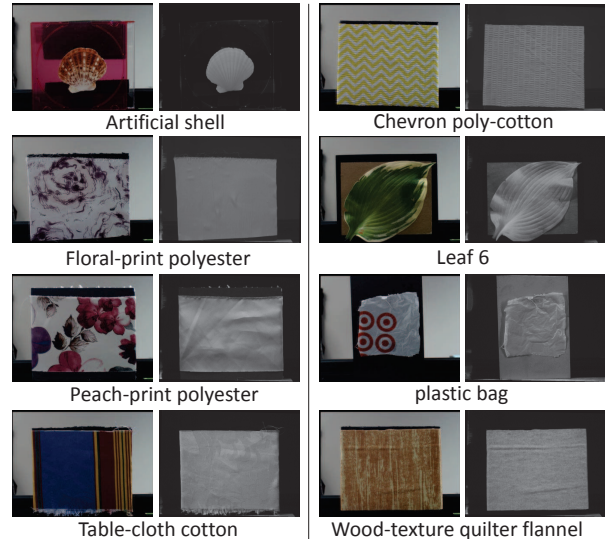


Figure 4. Differences in texture as seen in visible and NIR images. We show 8 examples from our 100 materials dataset. For each example, the left image shows visible and right image shows NIR image. Compared to the visible images, the NIR images show virtually no texture and most of the intensity gradients correspond to the shading due to surface geometry.

ing is provided in the supplementary material. All the images are captured under the same set of illumination directions. We capture a white paper as a reference target for lighting and include in the database. In Figure 5, the NIR images of our database is shown. The image set along with the BRDF and surface detail models are publicly available online¹.

3.3. Comparison of NIR and Visible Images

To compare the reflectance characteristics of the NIR images to visible images, we capture an RGB image using the visible camera with the same resolution as the NIR camera. We capture both NIR and visible images for 100 materials in Figure 5. In Figure 4, we show a representative set of 8 materials from our database. For each material, visible and NIR images are compared and we readily observe that the NIR images show less texture than visible images. The comparisons for the entire dataset are provided in the supplementary material. This allows us to assume that the BRDF is constant spatially across the material sample.

4. Joint Surface Detail and BRDF Estimation

If the surface normals of the material are known, then it is possible to directly observe and tabulate the BRDF or fit a parametric model. On the other hand, if the BRDF is known, photometric stereo can be used to estimate surface normals at every pixel. We jointly estimate both BRDF and

¹<http://rcv.kaist.ac.kr/gmchoe/project/NISAR/>

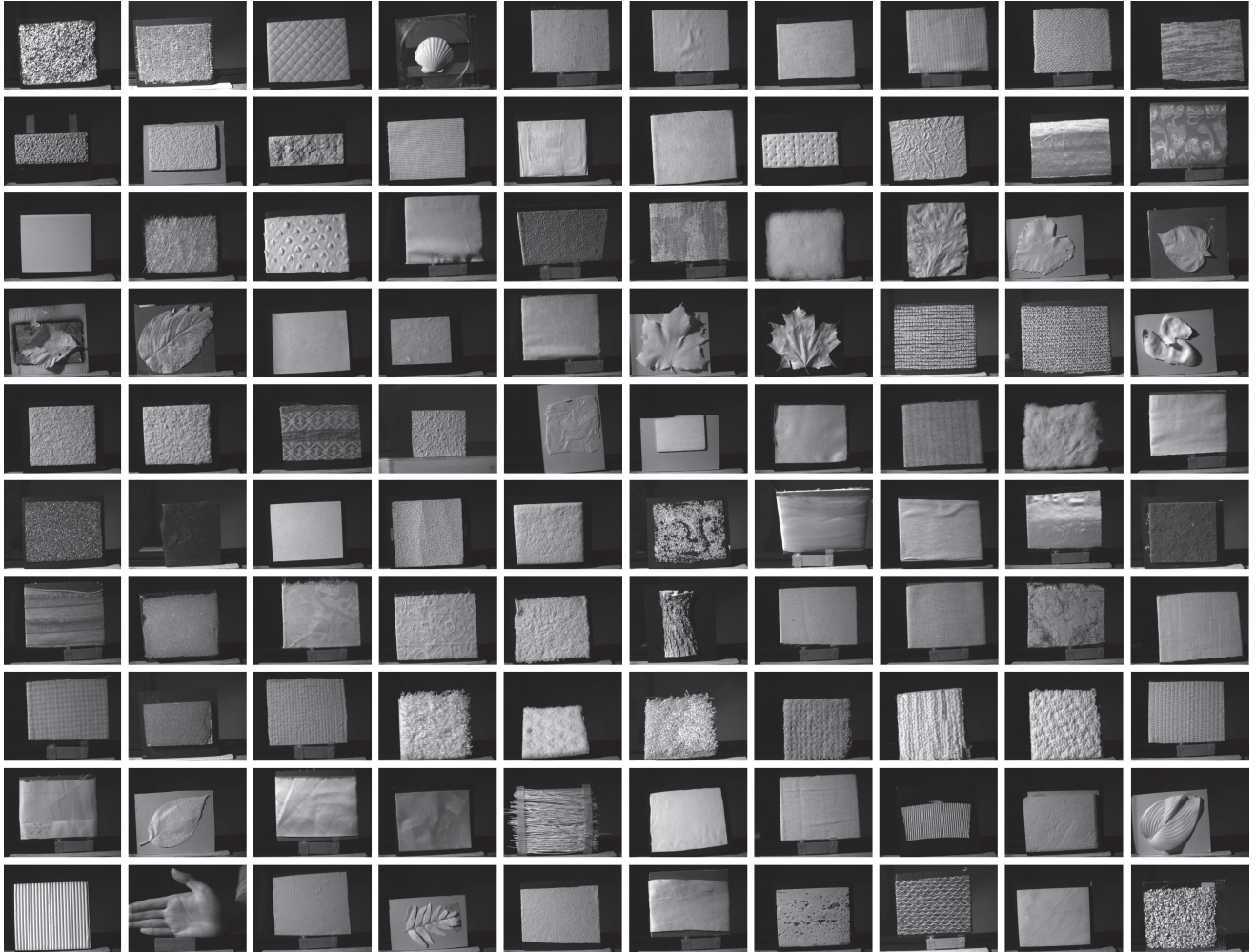


Figure 5. Our database consists of 100 real-world materials that include both natural and manmade and organic and inorganic samples. This is a superset of the materials in the original CURET database. Captured NIR images are shown. Full set of images under 12 lighting and 9 viewing angles, corresponding visible images and the BRDF and the surface detail models are available on-line. A complete listing of the materials is in the on-line web page.

surface detail using alternating optimization and show this approach converges for all the 100 materials.

The traditional image formation model relates observed radiance of an opaque scene point to the source radiance \mathbf{L} , BRDF ρ and local surface normal \mathbf{N}_x . We radiometrically calibrate the camera so the scene radiance is proportional to image intensity:

$$I_\psi(\mathbf{N}_x, \mathbf{L}) = \int \rho(\omega_i, \omega_o; \psi) \mathbf{L}(\omega_i) \max(0, \mathbf{N}_x \cdot \omega_i) d\omega_i, \quad (1)$$

The BRDF ρ is a function of incident angle ω_i and outgoing angle ω_o for specific material ψ .

4.1. Initial Estimation of Surface Detail

Since the materials in our database have measurable diffuse component, we initially assume that the BRDF $\rho(\omega_i, \omega_o)$ is invariant to the incident light directions or view-

ing directions in order to initialize the normal directions of the surface on the target samples. Using this Lambertian assumption, we apply traditional photometric stereo to compute the surface normals and albedo. Equation (1) can be written in a simplified matrix form with albedo α as:

$$\mathbf{I} = \alpha(\mathbf{N} \cdot \mathbf{S}), \quad (2)$$

where $\mathbf{N}_x \in \mathbf{N}$ and $\omega_i \in \mathbf{S}$. Setting $\mathbf{G} = \alpha\mathbf{N}$ and solve it using least squares yields:

$$\mathbf{G} = (\mathbf{S}^T \mathbf{S})^{-1} \mathbf{S}^T \mathbf{I}. \quad (3)$$

The surface orientation \mathbf{N} is obtained by normalizing matrix of \mathbf{G} and the albedo is set to be the norm, $\|\mathbf{G}\|$. We denote the solution normal matrix as \mathbf{N}^+ and compute the error \mathbf{e} to eliminate unreliable normals. The error is computed as an absolute deviation between the original intensity and the intensity computed from the solution normal,

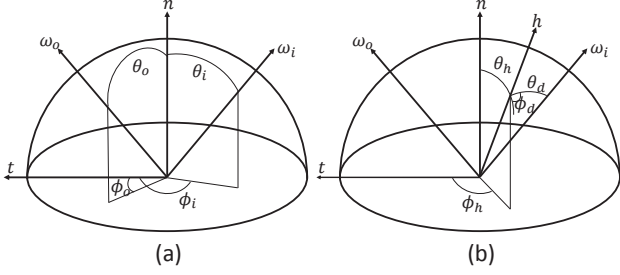


Figure 6. Coordinate systems. (a) Standard coordinate with respect to ω_i and ω_o . (b) Half-angle coordinate \mathbf{h} .

$\mathbf{e} = \|\mathbf{I} - \mathbf{N}^+ \cdot \mathbf{S}\|$. We set a threshold δ for selecting the reliable normals and the i th normal satisfying $e_i < \delta$ is used for our BRDF estimation. Although our BRDF assumption is most likely erroneous, we show that the pixel-wise surface normals we computed provide a strong initial guess for the optimization.

4.2. Parametric BRDF Model

The next step is to fit the BRDF model using the computed initial surface orientations. For this, we parameterize the angles and map the intensity values to the parameters. In our work, we use the commonly used half angle coordinates for BRDF [33, 27]. The coordinate frame is with respect to half angle \mathbf{h} which is a half vector of the incident angle ω_i and the outgoing angle ω_o (see Figure 6). The BRDF is now mapped to a function with respect to half angle parameters.

$$\rho(\omega_i, \omega_o) = \rho(f(\theta_h, \theta_d)), \quad (4)$$

where $\theta_h = \cos^{-1} \frac{\mathbf{N}_x \cdot \mathbf{h}}{\|\mathbf{N}_x\| \|\mathbf{h}\|}$ and $\theta_d = \cos^{-1} \frac{\omega_i \cdot \mathbf{h}}{\|\omega_i\| \|\mathbf{h}\|}$. By using the computed surface orientations and image intensities, we fit the data with respect to the half angle parameters, θ_h and θ_d . Note that in our work, we estimate the model for each discrete slice of θ_d . Since the camera is fixed and the object is rotated 9 different views, our setup leads $(108 \times 1200 \times 1600) \theta_h$ and 9 θ_d . We normalize the original NIR image \mathbf{I} by albedo α , and compute ρ for pixel i as follows:

$$\rho_i = \frac{\mathbf{I}_i}{\max(\mathbf{N}_{x,i} \cdot \mathbf{h}_i) \alpha_i}. \quad (5)$$

Here, we fit the data to a simple low-dimensional model parameterized by the half angles, which is sufficient to represent all the 100 materials. The model $\rho(\theta_h)$ for the specific slice of θ_d is defined as:

$$\rho(\theta_h) = \beta(\gamma)^{\theta_h} + \kappa. \quad (6)$$

To find the best β , γ , and κ , we use RANSAC [10] that best fits in 100 iterations by randomly sampling the data.

4.3. Iterative Process

We use the initial BRDF model and estimate the surface details via iterative optimization described in (7). Our goal

is to find the normal vector \mathbf{N}^* which minimizes the cost function (7). The cost function consists of the data term E_p and a smoothness term E_s ,

$$\mathbf{N}^* = \arg \min_{\mathbf{N}} (E_p(\mathbf{N}) + E_s(\mathbf{N})). \quad (7)$$

The data term is designed to minimize the difference between Intensity values of \mathbf{I} and the rendered intensity based on image formation model (1). We use least square error for the data term. Note that we clamp the negative values for rendered intensity, $\max(0, \mathbf{N}_{x,i} \cdot \mathbf{h}_i)$, and the normals are estimated for all 9 images with different viewing angles. The smoothness term is minimizing the difference of neighboring normals.

$$E_p(\mathbf{N}) = \sum_{i=1}^n \lambda (I_i - \rho_i(\theta_h) (\mathbf{N}_{x,i} \cdot \mathbf{h}_i))^2, \quad (8)$$

$$E_s(\mathbf{N}) = \sum_{i=1}^n \sum_{j \in M_i} (1 - \lambda) (\mathbf{N}_i - \mathbf{N}_j)^2, \quad (9)$$

where $\rho(\theta_h)$ is a estimated reflectance from (6) and M_i is pixel neighborhood of i . The optimization re-estimates the surface normal \mathbf{N}^* and updates \mathbf{N}^t as:

$$\mathbf{N}^t = s \mathbf{N}^{t-1} + (1 - s) \mathbf{N}^*, \quad (10)$$

where \mathbf{N}^t denotes the normal vector at updated time step and \mathbf{N}^{t-1} is the initial normal vector. s is a weight balancing the normals. We use the updated normal (10) for the BRDF model fitting again, as described in Section 4.2. After a few such iterations, we obtain the final BRDF and surface detail models.

Another approach to initialize the optimization is to assume the material patch is planar and compute the BRDF as an average over the patch [8]. This produces very sparse BRDF estimates and are generally clustered depending on the positioning of the light sources and the optimization failed to converge satisfactorily.

5. Experimental Results

For all our experiments, we set the parameters $\lambda = 0.2$, $\delta = 0.15$, $s = 0.6$. First, we present our results of surface detail and BRDF model estimation from material samples. We show 9 representative results in Figure 7 (see supplementary material for the rest). From the left column, we show (a) original NIR images, (b) surface normal map, (c) surface geometry from the reconstructed mesh, (d) albedo images, (e) estimated BRDF $\rho(\theta_h)$ for the slice of $\theta_d = 34^\circ$ which is plotted with red. The x-axis is θ_h and the y-axis is $\rho(\theta_h)$. Two hundred of randomly sampled data are shown as blue points. Please notice the vein structure of the leaf, the crumpled ridges of paper and the knits in artificial leather. Slight smoothing of the results are partly due to the smoothing term in the optimization and partly due to the fact that we do not model inter-reflections.

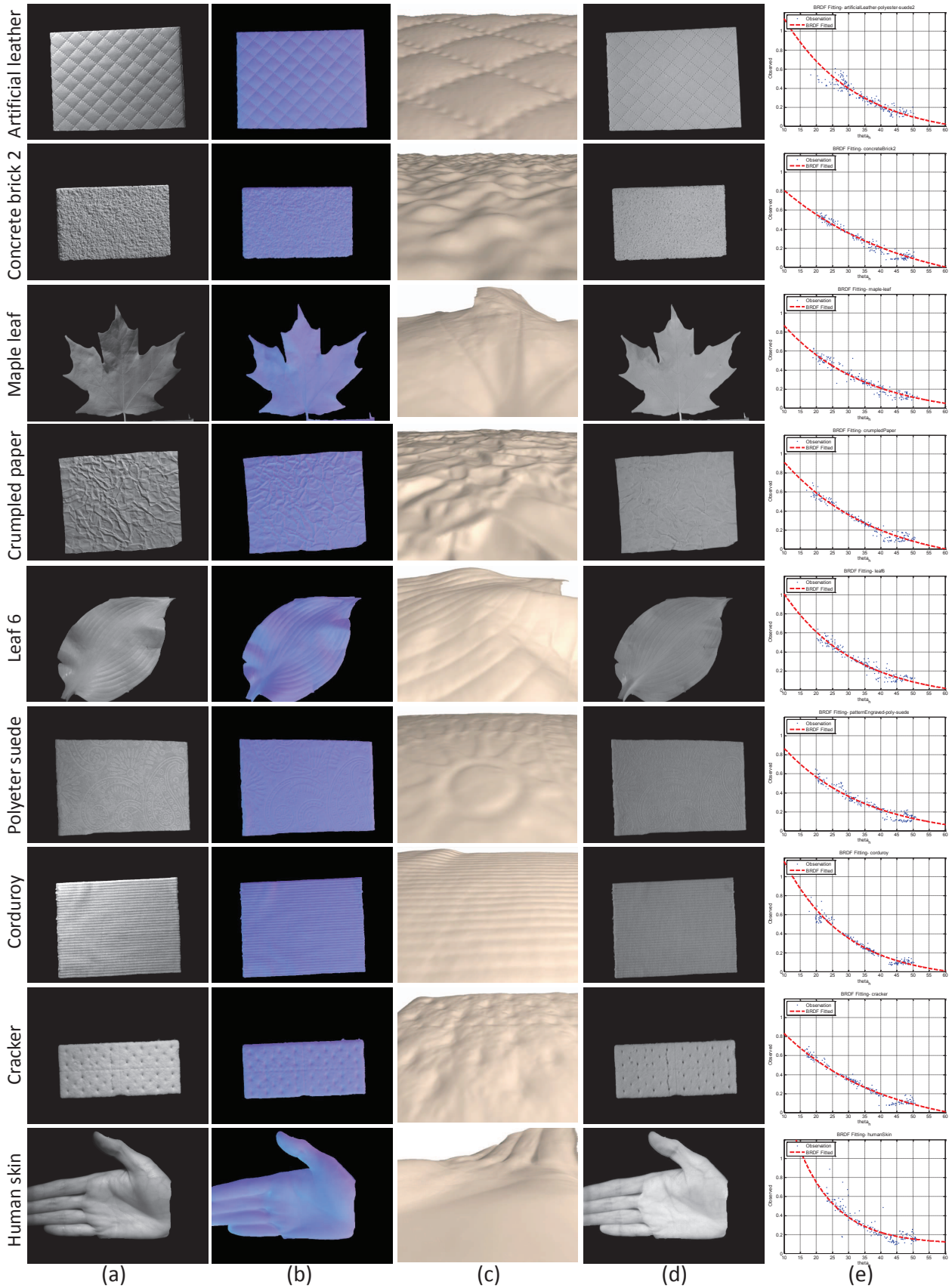


Figure 7. Nine examples out of 100 real-world samples are shown. (a) Near IR image. (b) Surface normal. (c) Fine surface detail. (d) Albedo. (e) Estimated $\rho(\theta_h)$ is plotted as a red curve. x-axis is θ_h and y-axis is ρ . 200 randomly sampled data are shown as blue points.

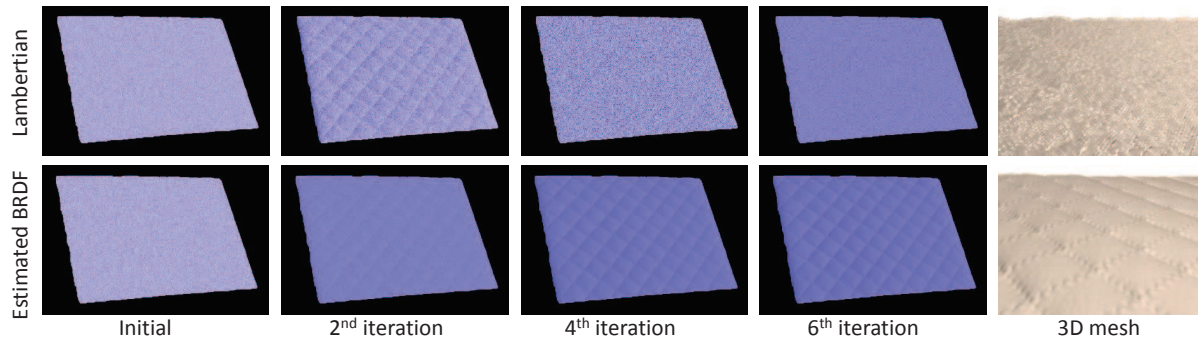


Figure 8. Normal map at each iteration for the Artificial leather. First row shows the normal estimation using Lambertian assumption and second row shows the normal estimation using our estimated BRDF. We use random normals for initialization. The rightmost column shows the reconstructed 3D mesh models.

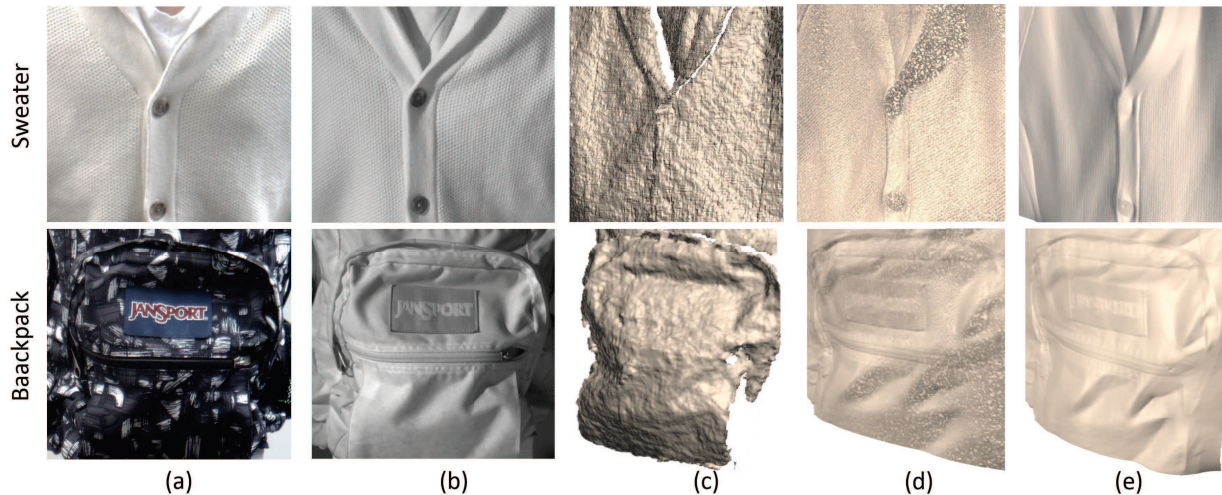


Figure 9. (a) Visible image. (b) Input NIR image. (c) Mesh from Kinect. (d) Mesh from our method using Lambertian assumption. (e) Mesh from our method using the estimated BRDF. First row is Sweater and second row is Backpack dataset.

Evaluation and Comparisons: In Figure 8, we demonstrate the iterations for a particular material sample. We display the normal maps at each iteration of our shape estimation method using both Lambertian and our measured BRDF. We initialize the normals with random values and observe how the optimization proceeds with each iteration. We did experiment using the Artificial leather sample under same parameter of $\lambda = 0.2$ for both cases. As iteration proceeds, the optimization using our BRDF converges better quality of solution. On the other hand, assuming the material to be Lambertian leads to the noisy and unstable results. The reconstructed 3D mesh of our method shows accurate surface detail. Once we capture the BRDF of materials, it is possible to use them within a shape from shading method to reconstruct the shapes of objects made of those materials. Here, example of Sweater and Backpack are shown. We use Microsoft Kinect for the comparison. The depth resolution of Kinect is 640×480 . To make a fair comparison, our input NIR image is down-sampled to the resolution of Kinect. For the sweater and backpack objects, qualitative comparisons between the Kinect mesh and the mesh from

our method are provided in Figure 9. We capture the fine knitting of the sweater and the wrinkles on the backpack. In Figure 9, we show (a) visible images, (b) our input NIR images, (c) the mesh from the Kinect, (d) the mesh from our method with Lambertian assumption and (e) the mesh from our method using BRDF from our database. The random initial normals are used for both (d) and (e). The mesh from Kinect cannot reconstruct fine detail and the mesh using the Lambertian assumption generates noisy and unstable results. On the other hand, the mesh from our method shows better quality.

Results of Shape from Shading with Measured BRDF:

The surface normal of arbitrary objects are estimated using the measured material BRDF. We use the known lighting direction (10th among 12) and the uniform value for normal initialization. We show the reconstructions of a person wearing jackets, sweaters and shirts made of different materials. These examples contain the fine geometry details on the surface and the BRDFs are complex and cannot be considered Lambertian. For better visualization, the result mesh models are rendered with a shader model and viewed

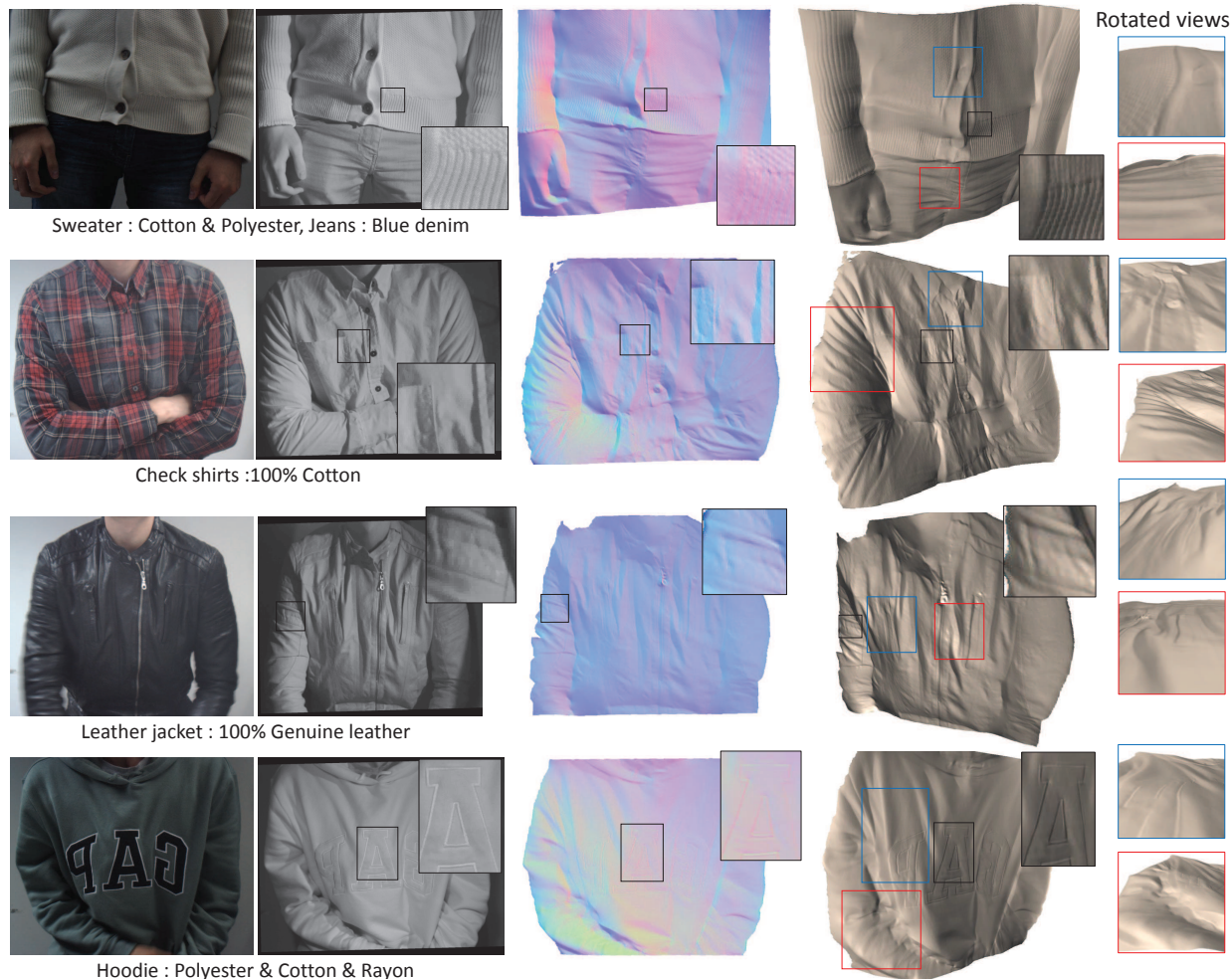


Figure 10. Results of our shape estimation using various real-world clothing - Sweater, Check shirts, Leather Jacket, and Hoodie. From the left, each column presents visible images, NIR images, Normal map and Reconstructed 3D mesh. Note that our method requires only a NIR image for the input, the visible images are provided for visual comparison of reflectance.

from a different angle. We use different BRDF models for each part of the target objects from our database (sweater: cotton-polyester, button: plastic, and jeans: blue denim BRDF). In Figure 10, notice the fine knitting of the sweater and wrinkles of jeans. We provide a video shape reconstruction of dynamic scene in the supplementary material. Check shirts (cotton) is also used. Even though it shows red-black check patterns in visible image, our input NIR image shows an uniform texture and only has "geometric" edges such as wrinkles. Thus, unlike the visible spectrum, it is possible to apply shape from shading assuming a uniform albedo in the NIR spectrum preserving fine details such as wrinkles and a pocket. For the Leather jacket, we use the BRDF model of the genuine leather. Our method reconstructs the wrinkles on the jacket and patterns on the arm. A hoodie is also used to evaluate our algorithm. The letter patch on the chest has a popped-out surface and once again the method reconstructs the fine detail as well as the wrinkles of the cloth.

6. Conclusion

We proposed a method for estimating the NIR BRDF and fine surface detail models of real-world materials. To the best of our knowledge, this is the first work to construct and provide a large dataset of NIR BRDFs and use it for shape from shading. We presented shape from shading results of various worn clothing by directly using our estimated BRDFs. Also we demonstrated that our results show improved quality over assuming a Lambertian model or Kinect depths on various challenging cases. In this work, we did not handle the inter-reflections which introduce some smoothing of the fine detail. Also our materials do not include very shiny metallic or mirrored objects, therefore our method has a limitation initializing the surface normal of those materials using Lambertian photometric stereo. Our dataset is publicly disseminated online.

***Acknowledgements** This research was supported by ONR Grant N00014-14-1-0595, NSF NRI grant IIS-1317749 and the Ministry of Trade, Industry & Energy and the Korea Evaluation Institute of Industrial Technology (KEIT) with the program number of 10060110.

References

- [1] M. Aittala, T. Weyrich, and J. Lehtinen. Two-shot svbrdf capture for stationary materials. *ACM Transactions on Graphics (TOG)*, 34(4):110, 2015. 1
- [2] N. Alldrin, T. Zickler, and D. Kriegman. Photometric stereo with non-parametric and spatially-varying reflectance. In *Proc. of Computer Vision and Pattern Recognition (CVPR)*, pages 1–8. IEEE, 2008. 1
- [3] J. T. Barron and J. Malik. Shape, albedo, and illumination from a single image of an unknown object. In *Proc. of Computer Vision and Pattern Recognition (CVPR)*, pages 334–341, 2012. 2
- [4] R. Basri, D. Jacobs, and I. Kemelmacher. Photometric stereo with general, unknown lighting. *International Journal of Computer Vision*, 72(3):239–257, 2007. 2
- [5] M. Brown and S. Süsstrunk. Multi-spectral sift for scene category recognition. In *Proc. of Computer Vision and Pattern Recognition (CVPR)*, pages 177–184. IEEE, 2011. 2
- [6] G. Choe, J. Park, Y.-W. Tai, and I. S. Kweon. Exploiting shading cues in kinect ir images for geometry refinement. In *Proc. of Computer Vision and Pattern Recognition (CVPR)*, 2014. 1, 2
- [7] R. Cook and K. Torrance. A reflectance model for computer graphics. *Computer Graphics*, 15:307–316, 1981. 2
- [8] K. J. Dana, B. Van Ginneken, S. K. Nayar, and J. J. Koenderink. Reflectance and texture of real-world surfaces. *ACM Transactions on Graphics (TOG)*, 18(1):1–34, 1999. 1, 2, 5
- [9] P. Debevec, T. Hawkins, C. Tchou, H.-P. Duiker, W. Sarokin, and M. Sagar. Acquiring the reflectance field of a human face. In *Proceedings of the 27th annual conference on Computer graphics and interactive techniques*, pages 145–156. ACM Press/Addison-Wesley Publishing Co., 2000. 2
- [10] M. A. Fischler and R. C. Bolles. Random sample consensus: a paradigm for model fitting with applications to image analysis and automated cartography. *Communications of the ACM*, 24(6):381–395, 1981. 5
- [11] A. Ghosh, S. Achutha, W. Heidrich, and M. O’Toole. Brdf acquisition with basis illumination. In *Proc. of Int’l Conf. on Computer Vision (ICCV)*, pages 1–8. IEEE, 2007. 2
- [12] D. Goldman, B. Curless, A. Hertzmann, and S. Seitz. Shape and spatially-varying brdfs from photometric stereo. In *Proc. of Int’l Conf. on Computer Vision (ICCV)*, October 2005. 2
- [13] H. Ha, J. Park, and I. S. Kweon. Dense depth and albedo from a single-shot structured light. In *3D Vision (3DV), 2015 International Conference on*, pages 127–134. IEEE, 2015. 2
- [14] Y. Han, J.-Y. Lee, and I. Kweon. High quality shape from a single rgb-d image under uncalibrated natural illumination. In *Proc. of Int’l Conf. on Computer Vision (ICCV)*, 2013. 2
- [15] S. M. Haque, A. Chatterjee, and V. M. Govindu. High quality photometric reconstruction using a depth camera. In *Proc. of Computer Vision and Pattern Recognition (CVPR)*, pages 2283–2290. IEEE, 2014. 2
- [16] B. K. P. Horn and M. J. Brooks. *Shape from shading*. MIT Press, Cambridge, MA, USA, 1989. 2
- [17] R. Huang and W. A. Smith. Shape-from-shading under complex natural illumination. In *Image Processing (ICIP), 2011 18th IEEE International Conference on*, pages 13–16. IEEE, 2011. 2
- [18] K. Ikeuchi and B. K. Horn. Numerical shape from shading and occluding boundaries. *Artificial intelligence*, 17(1):141–184, 1981. 2
- [19] M. K. Johnson and E. H. Adelson. Shape estimation in natural illumination. In *Proc. of Computer Vision and Pattern Recognition (CVPR)*, pages 2553–2560. IEEE, 2011. 2
- [20] J. M. Kaldor, D. L. James, and S. Marschner. Simulating knitted cloth at the yarn level. In *ACM Transactions on Graphics (TOG)*, volume 27, page 65. ACM, 2008. 2
- [21] C. Kerl, M. Souiai, J. Sturm, and D. Cremers. Towards illumination-invariant 3d reconstruction using tof rgb-d cameras. In *3D Vision (3DV), 2014 2nd International Conference on*, volume 1, pages 39–46. IEEE, 2014. 1, 2
- [22] J. Lambert. *Photometria sive de mensura de gratibus luminis, colorum et umbrae*. eberhard klett, augsburg, 1760. W. Engleman, *Lambert’s Photometrie*. Leipzig, 127:128, 1982. 2
- [23] K. M. Lee and C. Kuo. Shape from shading with linear triangular element surface model. *IEEE Trans. Pattern Anal. Mach. Intell.*, 15(8):815–822, 1993. 2
- [24] H. Lensch, J. Kautz, M. Goesele, W. Heidrich, and H.-P. Seidel. Image-based reconstruction of spatial appearance and geometric detail. *ACM Transactions on Graphics (TOG)*, 22(2):234–257, 2003. 2
- [25] Y. M. Lu, C. Fredembach, M. Vetterli, and S. Süsstrunk. Designing color filter arrays for the joint capture of visible and near-infrared images. In *Image Processing (ICIP), 2009 16th IEEE International Conference on*, pages 3797–3800. IEEE, 2009. 2
- [26] S. R. Marschner. *Inverse rendering for computer graphics*. PhD thesis, Citeseer, 1998. 1
- [27] W. Matusik, H. Pfister, M. Brand, and L. McMillan. A data-driven reflectance model. *ACM Transactions on Graphics (TOG)*, 22(3):759–769, July 2003. 1, 2, 5
- [28] F. Nicodemus, J. Richmond, J. Hsia, I. Ginsberg, and T. Limperis. Geometric considerations and nomenclature for reflectance, volume 161 of monograph. *National Bureau of Standards (US)*, 1977. 1
- [29] K. Nishino. Directional statistics brdf model. In *Proc. of Int’l Conf. on Computer Vision (ICCV)*, pages 476–483. IEEE, 2009. 2
- [30] M. Oren and S. K. Nayar. Generalization of the lambertian model and implications for machine vision. *International Journal of Computer Vision*, 14(3):227–251, 1995. 1, 2
- [31] B. T. Phong. Illumination for computer generated pictures. *Communications of the ACM*, 18(6):311–317, 1975. 2
- [32] D. Rufenacht, C. Fredembach, and S. Süsstrunk. Automatic and accurate shadow detection using near-infrared information. *IEEE Trans. Pattern Anal. Mach. Intell.*, 36(8):1672–1678, 2014. 1, 2
- [33] S. M. Rusinkiewicz. A new change of variables for efficient brdf representation. In *Rendering techniques 98*, pages 11–22. Springer, 1998. 2, 5
- [34] N. Salamati, Z. Sadeghipoor Kermani, and S. Süsstrunk. Analyzing Near-infrared Images for Utility Assessment. In *IS&T/SPIE Electronic Imaging: Human Vision and Electronic Imaging*, volume 7865. SPIE-Int Soc Optical Engineering, Po Box 10, Bellingham, Wa 98227-0010 Usa, 2011. 2
- [35] C. Schlick. An inexpensive brdf model for physically-based rendering. In *Computer graphics forum*, volume 13, pages 233–246, 1994. 2
- [36] H. Tang, X. Zhang, S. Zhuo, F. Chen, K. N. Kutulakos, and L. Shen. High resolution photography with an rgb-infrared camera. In *ICCP*, pages 1–10. IEEE, 2015. 2
- [37] K. E. Torrance and E. M. Sparrow. Theory for off-specular reflection from roughened surfaces. *JOSA*, 57(9):1105–1112, 1967. 1, 2
- [38] P. Tsai and M. Shah. Shape from shading using linear-approximation. *IVC*, 12(8):487–498, 1994. 2
- [39] G. J. Ward. Measuring and modeling anisotropic reflection. *ACM SIGGRAPH Computer Graphics*, 26(2):265–272, 1992. 2
- [40] L.-F. Yu, S.-K. Yeung, Y.-W. Tai, and S. Lin. Shading-based shape refinement of rgb-d images. In *Proc. of Computer Vision and Pattern Recognition (CVPR)*, 2013. 2
- [41] R. Zhang, P.-S. Tsai, J. E. Cryer, and M. Shah. Shape from shading: A survey. *IEEE Trans. Pattern Anal. Mach. Intell.*, 21(8):690–706, 1999. 2
- [42] Q. Zheng and R. Chellappa. Estimation of illuminant direction, albedo, and shape from shading. *IEEE Trans. Pattern Anal. Mach. Intell.*, 13(7):680–702, 1991. 2